Journal of Physics D:
Applied Physics

PURPOSE-LED PUBLISHING™

PAPER

Magneto-transport and magnetocaloric properties of highly doped (Ga,Mn)As DMS confined systems

To cite this article: K Lakaal *et al* 2026 *J. Phys. D: Appl. Phys.* **59** 105001

View the article online for updates and enhancements.

You may also like

- Collapse of ferromagnetism in (Ga, Mn)As at high hole concentrations
Y J Cho, X Liu and J K Furdyna
- Hole concentration in a diluted ferromagnetic semiconductor
Raimundo R dos Santos, Luiz E Oliveira and J d'Albuquerque e Castro
- Hole density of ferromagnetic semiconductor (Ga, Mn)As studied via pulsed high magnetic field
K K Cong, Y Ji, Z C Xia et al.



This content was downloaded from IP address 152.74.34.153 on 29/09/2026 at 12:32

IOP Publishing J. Phys. D: Appl. Phys. 59 (2026) 105001 https://doi.org/10.1088/1361-6463/ae4b4b

Journal of Physics D: Applied Physics

Check for updates

PAPER

RECEIVED
1 October 2025

REVISED
9 February 2026

ACCEPTED FOR PUBLICATION
27 February 2026

PUBLISHED
10 March 2026

Magneto-transport and magnetocaloric properties of highly doped (Ga,Mn)As DMS confined systems

K Lakaal[1], L M Pérez[2], V Prasad[3], D Laroze[4], V Chaudhary[5], W J Pasek[5], A En Naciri[6], A El Fatimy[5] and E Feddi[5,*]

[1] Group of Optoelectronic of Semiconductors and Nanomaterials, ENSAM, Mohammed V University, Rabat, Morocco
[2] Departamento de Ingeniería Industrial y de Sistemas, Universidad de Tarapacá, Casilla 7D, Arica, Chile
[3] Department of Physics, Swami Shraddhanand College, University of Delhi, Delhi-110036, India
[4] Instituto de Alta Investigación, Universidad de Tarapacá, Casilla 7 D, Arica 1000000, Chile
[5] School of Applied and Engineering Physics, Mohammed VI Polytechnic University, Lot 660, Hay Moulay Rachid Ben Guerir 43150, Morocco
[6] LCP-A2MC, Université de Lorraine, ICPM, 1 Bd Arago, 57070 Metz, France
[*] Author to whom any correspondence should be addressed.

E-mail: e.feddi@um5r.ac.ma

Keywords: spintronics, antiferromagnetic, diluted magnetic semiconductors, magnetization, magnetic susceptibility, persistent current

Abstract

This work investigates the magneto-transport and magnetocaloric properties of interacting holes in highly Mn-doped (Ga,Mn)As. The model includes hole–longitudinal optical phonon coupling and analyzes the effects of temperature (0–50 K) and magnetic field (−5 to 5 T). The energy spectrum is obtained from the Schrödinger equation, and thermodynamic properties are evaluated using Boltzmann–Gibbs statistics. The formalism and numerical calculation are applied to ($Ga_{0.97}Mn_{0.03}As$) containing 3% Mn. The magnetic susceptibility behavior indicates that antiferromagnetic interactions are associated with ferromagnetic order in (Ga,Mn)As under certain conditions. Additionally, both the adiabatic temperature change(ΔT_{ad}) and the magnetic entropy change(ΔS_M) are calculated. The minimum of magnetic entropy change ($\Delta S_M/K_B$) is found to increase linearly with applied magnetic field and provides −0.54 for the field value of 2 T. In addition, the persistent current in the presence of magnetic fields is also investigated considering the role of the hole–hole interactions. Our calculations highlight two interesting results: a substantial reduction in the current results from an increase in the magnetic field at low temperatures on the one hand, and on the other hand, the interaction between holes induces an increase in the overall amplitude of the current.

1. Introduction

Nowadays, quantum electronics has witnessed significant attention due to the development of novel semiconducting materials and advanced fabrication techniques [1–3]. Novel materials combining magnetic and semiconducting characteristics in confined systems open new opportunities for exploiting electron spin in electronic devices for next-generation information processing, communication, and storage technologies [4]. The spin effects are not exploited in conventional semiconductor electronic devices. The most used integrated circuits employ nonmagnetic materials such as Si, Ge, and GaAs, where the energy of charge carriers is independent of the spin states. However, it was demonstrated that the devices working with both the electrical and spin properties (spintronic devices) allow the development of new optoelectronic devices having fascinating properties [5]. Indeed, compared to the motion of the charge carriers (electrons and holes), the spin can be switched quickly between two states; thus, spintronic components are expected to work faster without heating losses in comparison to current electronics. This concept has led to the development of several novel devices, including giant magnetoresistance sensors, spin-polarized transistors, spin-polarized light emitters, magnetic tunnel junctions, spin-transfer torque, and the spin Hall effect, with enhanced functionality [5–9].

© 2026 IOP Publishing Ltd. All rights, including for text and data mining, AI training, and similar technologies, are reserved.

However, the fabrication of these devices for future electronics requires materials with spintronic properties. Numerous classes of materials, such as half-metallic ferromagnets (CrO_2), spinels (Fe_3O_4), perovskites [(La,Sr)MnO_3], magnetic semiconductors (EuO, EuS, (Ga,Mn)As and CrAs), heusler alloys (NiMnSb), perpendicularly anisotropic materials (CoFeB/MgO/CoFeB), and antiferromagnetic materials, etc have been explored for spintronic and next-generation information technology devices [10]. On the other hand, doping with magnetic impurities provides another way to obtain semiconductors with spintronic properties. In group II–VI semiconductors, where the cation's valence band coincides with the valence band of magnetic ions (Mn,Cr), antiferromagnetic interactions with very low Curie temperatures are fundamental [11]. Additionally, the Mn-doped group III–V semiconductors—so-called diluted magnetic semiconductors (DMSs)—such as (Ga,Mn)N, (Ga,Mn)As, (Zn,Mn)Te and (Ge,Mn), have attracted considerable attention in last few years due to their potential applications in spintronics [12–14]. Their magnetic behavior depends on several factors.

The ferromagnetism in DMS of group III–V materials remains controversial and needs further understanding. Multiple theoretical models have been put forward to elucidate their magnetic behavior; notably, the Ruderman–Kittel–Kasuya–Yosida (RKKY) model describes magnetism arising from indirect exchange interactions between localized d- and f-shell electron spins [15, 16]. The alternative Zener model is based on the valence holes occupying p-orbitals [9, 17]. Both models point out the importance of coupling between the carriers and localized spins to the overall functionality of the material.

In GaAsMn, the Mn impurities have an unpaired electron with a magnetic moment at low Mn concentrations. However, these magnetic moments are randomly oriented, giving a net zero magnetic moment. At higher Mn concentrations, the magnetic moments of the Mn impurities align with each other, resulting in ferromagnetic behavior [18]. Many studies have shown that a high concentration of holes can lead to the formation of local magnetic moments through a process called carrier-mediated ferromagnetism [19]. The system exhibits a transition from ferromagnetic to antiferromagnetic behavior at even higher hole concentrations [20]. This transition occurs because the holes mediate the interactions between the Mn ions, which favors the antiparallel alignment of the magnetic moments. Specifically, the holes can induce an indirect exchange coupling between Mn ions, in which a hole on one Mn ion can generate a local magnetic moment that interacts antiferromagnetically with the magnetic moment of an adjacent Mn ion. Moreover, the relationship between hole concentration and antiferromagnetic behavior in GaAsMn is complex and depends on both Mn concentration and temperature. It has generally been observed that increasing the hole concentration can lead to the transition from ferromagnetic to antiferromagnetic behavior in (Ga_{1-x} Mn_xAs) DMS system.

In the doping range $0.015 \leqslant x \leqslant 0.071$, the system undergoes a transition to a ferromagnetic state, with the critical temperature $\mathcal{T}_c(x)$ strongly dependent on doping and reaching a maximum of 110 K for $x = 0.053$ [21]. Similar to previous observations, this ferromagnetic ordering is attributed to an exchange coupling between localized Mn magnetic moments mediated by holes, whose strength is governed by the hole concentration [22]. These findings indicate that the origin of the ferromagnetic–antiferromagnetic discrepancy, arising from the interplay between Mn doping density and hole concentration, warrants further detailed study. As pointed out by Matsukura *et al* [19], such discrepancies may result from the compensation of Mn acceptors by deep donor defects, such as As antisites, commonly present in low-temperature-grown GaAs [23]. Thus, the relation between the critical temperature, Mn composition in (Ga_{1-x} Mn_xAs), and hole concentration is still not evident, but undoubtedly dependent on the experimental conditions [20, 24–29]. A widely accepted model assumes that Mn ions couple to holes through a local antiferromagnetic Kondo-like exchange interaction between their magnetic moments [8, 16, 21]. The induced polarization of the hole subsystem is believed to mediate an effective ferromagnetic coupling between Mn moments in the low-doping regime.

The experimental measurements by Ohno *et al* have shown that the hole and Mn concentrations are of the same order of magnitude, and the layered sample in the mentioned work exhibits an anomalous Hall effect [13]. Using DFT computation, Da Silva *et al* have demonstrated that the total energy of GaAsMn presents a predominant p-like character and interacts with the fully polarized Mn d5-electrons [30]. The theoretical calculations indicate that the effective Mn–Mn coupling does not follow an RKKY-type interaction but remains ferromagnetic, arising from the antiferromagnetic coupling between each Mn spin and the hole carriers. Complementary studies have revealed magnetic influences extending up to room temperature at Fe/(Ga,Mn)As interfaces [31]. The magnetic behavior of Mn atoms in epitaxial Fe/(Ga,Mn)As heterostructures was analyzed in detail by Sperl [32]. Furthermore, Zhang showed through first-principles calculations that shifting Mn dopants toward the edge of bare nanowires significantly lowers the Mn formation energy [33]. Also, the transition from antiferromagnetic to ferromagnetic behavior was observed in the mentioned work. Recently Bardrtdinov *et al* [34] have shown that the

hole-phonon coupling can significantly influence magnetic properties, potentially dominating over many-body effects, especially in materials where strong coupling exists, leading to phenomena like spin–lattice interactions and modifications of exchange interactions. The interaction between spin-polarized charge carriers (like holes) and phonons can mediate spin–lattice interactions, leading to the renormalization of exchange interactions (the strength of magnetic interactions between spins). Zhou *et al* [35] showed that electron–hole interactions strongly affect charge and energy transport in various electronic and photonic systems. Despite progress in phonon-related electronic dynamics, probing carrier effects on phonon heat transport at room temperature remains difficult. Here, this effect is examined using a modified transient thermal grating technique. Also, the interaction between spin-polarized charge carriers (like holes) and phonons can mediate spin-lattice interactions, leading to renormalization of exchange interactions (the strength of magnetic interactions between spins), all these and many other studies show that electron–hole interactions are essential to understand the physics behind magnetic properties of Quantum dots. In materials with strong hole-phonon coupling, the effects of this coupling on magnetic properties can become more important than those arising from many-body interactions (interactions between multiple electrons or holes) [36]. There have been studies which underscore the critical role of hole-phonon coupling in determining the magnetic properties of (Ga,Mn)As, particularly in scenarios where it dominates over many-body interactions [37, 38]

Let us suppose that we have a highly p-doped (Ga_{1-x} Mn_xAs) DMS and thus the hole density is critical. It is well known that holes have strong spin–orbit coupling (SOC), which allows control of the spin states of holes. These hole states contribute to many spintronic phenomena, such as the design of qubits [39] and the overcoming of decoherence [40, 41]. The significance of hole states in confined systems has been well documented in the literature through both theoretical and experimental studies [42]. However, the existing studies on multihole system including both coulomb interaction between holes and interactions with longitudinal optical phonon (LO) are contradictory [43–45].

Xiang *et al* [46] recently studied two-dimensional hole gases in quantum wells incorporating spin–orbit coupling, revealing that hole–hole interaction terms contributing to SOC are crucial for the spin properties of hole gases. Complementary experimental work by Tai *et al* [47] demonstrated that two-dimensional hole gases can be efficiently tuned by electrostatic gating, resulting in high mobility. These advances indicate that the traditional drawbacks of hole-based devices compared to electron-based technologies may be overcome, paving the way toward commercially viable hole-state devices [48]. Consequently, investigations into hole-based quantum structures have gained significant momentum. Recent studies include experimental probing of low-temperature transport in single-hole quantum dots by Delaforce *et al* [49], as well as theoretical exploration of two-dimensional quantum dot arrays with single-hole occupancy as a candidate architecture for quantum computation by van Riggelen *et al* [50]. These studies validate the importance of hole states in the semiconductor QD as promising criteria for quantum information [51]. An important advantage of hole-based systems lies in the strong anisotropy observed in self-assembled quantum dots, which originates from the p-type orbital nature of holes rather than from electron states. A detailed analysis of hole energies and wavefunctions is therefore essential, as these properties are crucial for the performance of hole-based devices.

Studying a two-hole system, instead of the experimentally relevant case with about 10^2 holes, provides fundamental insight into electronic and magnetic interactions. This minimal model clarifies how interactions between magnetic impurities and holes give rise to magnetic moments, spin dynamics, and exchange effects. Even though the experimental situation involves many more holes, understanding the basic interaction mechanisms provides a foundation for predicting and interpreting more complex behavior in larger systems. The interactions found in a two-hole system can sometimes be scaled up to predict the behavior of a larger system. Although many-body effects intensify, some aspects like average exchange interactions per hole may scale in a predictable way. If the interaction energy per hole pair remains nearly constant as the number of holes increases, results from a two-hole system may qualitatively describe larger systems. However, many-body effects can cause deviations. The two-hole framework can be extended by explicitly including many-body interactions. Although these calculations are more complex, they can build upon the two-hole model by introducing interactions between additional holes and refining models to include phenomena such as screening, correlation, and disorder.

To understand the behavior of hole–hole interaction in the GaMnAs DMS with a high concentration of Mn, with corresponding high density of holes, we develop a simple model considering a two hole–hole system in the framework of the effective mass approximation. To be more precise in the experimental limit, we have included hole–LO–phonon interactions using Fröhlich formalism. We performed a detailed analysis of a two-hole parabolic quantum dot, determining both the energy levels and associated wave functions in the presence of a magnetic field. We analyze the magnetic and thermodynamic properties of the system namely, the magnetization, magnetic susceptibility, specific heat, and entropy.

Based on the arguments above, we focus on magneto-transport and magnetocaloric properties in low-temperature regimes and under moderate magnetic fields. The paper is organized as follows: section 2 deals with the theoretical model and the results are discussed in detail in section 3. Concluding remarks are presented in the last section.

2. Theory and model

2.1. Hamiltonian of the system

In this work, we focus on the case of a DMS with a Mn concentration of 3%, a value representative of typical (Ga, Mn)As samples exhibiting ferromagnetic behavior at low temperatures. This concentration does not appear explicitly in the formalism but is taken into account phenomenologically through the effective parameters used in our model, as summarized in table 1. The exchange interaction, carrier density, and spin splitting are chosen to represent the effective magnetic and electronic environment at the considered Mn concentration. This approach relies on a mean-field description in which randomly distributed Mn ions form an effective uniform magnetic background. Given the statistical nature of Mn incorporation and the relatively low doping regime (3%), spatial fluctuations and clustering effects can be neglected to a first approximation. Therefore, incorporating the concentration through effective parameters allows us to retain the essential physics while keeping the model tractable for analytical and numerical treatment. We emphasize that this approach is consistent with previous theoretical works in the field, where specific Mn concentrations are accounted for by calibrating model parameters based on experimental results or detailed *ab initio* calculations. For clarity, we now explicitly state in this section that the 3% Mn content is reflected in the choice of parameters, ensuring that the simulated system corresponds to realistic experimental conditions.

First, we outline the theoretical approach for calculating the energy levels of two interacting holes in a 2D quantum system subjected to a magnetic field $\overrightarrow{B} = (0,0,B)$ defined in the Lorentz gauge by the vector potential $\overrightarrow{A} = \frac{1}{2}(\overrightarrow{B} \times \overrightarrow{r})$, as demonstrated in figure 1. We can calculate the system's energy through the solution of the time-independent Schrödinger equation $\hat{\mathcal{H}}|\Psi\rangle = E|\Psi\rangle$, taking the interaction between hole and LO–phonons into account. The Hamiltonian of the system is defined as follows:

$$\hat{\mathcal{H}} = \frac{1}{2m^*_{hh}} \sum_{j=1}^{2} \left(\overrightarrow{p}_j - \frac{e\overrightarrow{A}_j}{c} \right)^2 + \frac{1}{2} m^*_{hh} \omega_0^2 \sum_{j=1}^{2} r_j^2 + \frac{\mathrm{e}^2}{\varepsilon_\infty \left| \overrightarrow{r}_1 - \overrightarrow{r}_2 \right|} + \frac{1}{2} g^* B \mu_B \sum_{j=1}^{2} \hat{\sigma}_{z,j} + \sum_{\vec{q}} \hbar\omega_{\mathrm{LO}} \hat{a}^+_{\vec{q}} \hat{a}_{\vec{q}}$$
$$+ \sum_{\vec{q}} \sum_{j=1}^{2} \left[\widehat{a}_{\overrightarrow{q}} V_{\overrightarrow{q}} (\exp(i\overrightarrow{q} \cdot \overrightarrow{r_j}) + H.c \right]. \tag{1}$$

Here, the first four terms on the right-hand side represent the Hamiltonian of the two-interacting holes in a 2D parabolic potential, with $\hbar\omega_0$ being the energy scale of the parabolic confinement. Further, m^*_{hh} is the effective mass of the heavy hole ($\overrightarrow{r_j}$), $\overrightarrow{p_j}$ represents the momentum of the jth hole, c denotes the speed of light in vacuum. The hole–hole interaction is represented by the third term in equation (1), where ε_∞ denotes the dielectric constant at high frequencies. The Zeeman contribution corresponds to the fourth term in equation (1), where g^* denotes the effective Landé factor, $\mu_B = \frac{e\hbar}{2m_0 c}$ is the Bohr magneton, and $\hat{\sigma}_z$ represents the Pauli spin matrix. The remaining terms in equation (1) describe the phonon kinetic energy and the interaction Hamiltonian between holes and phonons within the Fröhlich framework. Phonons with wave vector $\vec{q}$ are created and annihilated by the operators $\hat{a}^\dagger_{\vec{q}}$ and $\hat{a}_{\vec{q}}$, respectively, ω_{LO} denotes the longitudinal optical phonon frequency, and $V_{\vec{q}}$ characterizes the coupling strength. To solve the Schrödinger equation, center-of-mass and relative coordinates are introduced. The polaronic contribution can be simplified using the Lee-Low Pines (LLP) method [52]. Thus, the Hamiltonian of the system can be separated into two independent parts, commuting with each other $[\mathcal{H}^{\mathrm{rel}}, \mathcal{H}^{\mathrm{cm}}] = 0$, where $\mathcal{H}^{\mathrm{rel}}$ is the Hamiltonian of the relative motion and $\mathcal{H}^{\mathrm{cm}}$ is the Hamiltonian of the center-of-mass motionand. Under this condition the total Hamiltonian can be expressed as:

$$\mathcal{H} = \mathcal{H}^{\mathrm{rel}} + \mathcal{H}^{\mathrm{cm}}. \tag{2}$$

Consequently, the system's energy spectrum can be expressed as follows:

$$E = E^{\mathrm{rel}} + E^{\mathrm{cm}}. \tag{3}$$

The Hamiltonian associated with relative motions ($\mathcal{H}^{\mathrm{rel}}$) takes the following form:

$$\mathcal{H}^{\mathrm{rel}} = \mathcal{H}^0_{\mathrm{rel}} + V^{\mathrm{int}}. \tag{4}$$

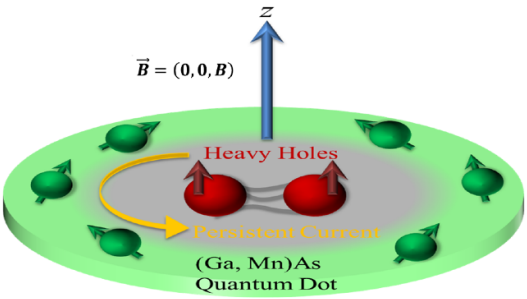


Figure 1. The schematic illustration of the model system. Two interacting heavy holes are confined in a two-dimensional parabolic quantum dot formed in doped (Ga,Mn)As. Localized Mn magnetic moments (represented in green color) are randomly distributed inside the dot and interact with the hole spins via an effective exchange coupling. An external magnetic field $\rightarrow B = (0, 0, B)$ is applied perpendicular to the plane of confinement, inducing orbital quantization and persistent current. The vector potential is taken in the symmetric gauge $\rightarrow A = \frac{1}{2}(\rightarrow B \times \rightarrow r)$.

Table 1. Physical parameters of (Ga,Mn)As (3% Mn) considered in this work [60–65].

Material	ε_0	ε_∞	E_g (eV)	m_h^*/m_0	m_e^*/m_0	$\hbar\omega_{\rm TO}$ (meV)	$\hbar\omega_{\rm LO}$ (meV)	a^* (Å)	R^* (meV)	g^*	S
(Ga,Mn)As	13.99	11.8	1.50	0.5	0.067	36.22	33.29	25	24.4	2	5/2

Here, $\mathcal{H}^0_{\rm rel}$ is defined the unperturbed relative-motion Hamiltonian. The operator $V^{\rm int}$ on the other hand, incorporates both the Coulombic contribution and the phonon–hole interaction.

where:

$$\mathcal{H}^0_{\rm rel} = \frac{p_r^2}{2\mu} + \frac{1}{2}\mu\Omega^2 r^2 - \frac{1}{2}\omega_c L_z + \alpha_{\rm LO}\hbar\omega_{\rm LO}, \tag{5}$$

here $\mu = m^*_{hh}/2$ and $\Omega = \sqrt{\omega_0^2 + \frac{\omega_c^2}{4}}$, $\omega_c = \frac{eB}{m^*_{hh}c}$, L_z is the angular momentum associated with relative motions.

The term describing the Coulombic potential and phonon–hole interaction can be obtained from equation (1) by using the well-known LLP transformation [53]. It can be written as :

$$V^{\rm int} = \frac{e^2}{\varepsilon_\infty r} - \frac{2\alpha_{\rm LO}\hbar\omega_{\rm LO}}{u_{\rm LO} r}\left(1 - e^{-u_{\rm LO} r}\right) - \alpha_{\rm LO}\hbar\omega_{\rm LO} e^{-u_{\rm LO} r}, \tag{6}$$

where the inverse length $u_{\rm LO}$ is given by the relation $(\frac{\hbar^2 u_{\rm LO}^2}{2M_0} = \hbar\omega_{\rm LO})$ and

$$\alpha_{\rm LO} = \frac{e^2}{2\hbar\omega_{\rm LO}}\left(\frac{2M_0\omega_{\rm LO}}{\hbar}\right)^{1/2}\left(\frac{1}{\varepsilon_\infty} - \frac{1}{\varepsilon_0}\right), \tag{7}$$

represents the hole–LO–phonon coupling.

According to this approach, the wave function of the unperturbed system, $\mathcal{H}^0_{\rm rel}$ can easily be identified:

$$\Psi_{n,m}(r, \Phi) = \frac{1}{\sqrt{2\pi}} e^{(im\Phi)} f_{n,m}(r), \tag{8}$$

where $f_{n,m}(r)$ is the normalized radial wave function given by:

$$f_{n,m}(r) = \sqrt{\frac{2a^2 n!}{(n + |m|)!}}\,(ar)^{|m|} L_n^{|m|}\left(a^2 r^2\right) \exp\left(-\frac{a^2 r^2}{2}\right). \tag{9}$$

Here n and m are the radial and the angular momentum quantum numbers, respectively. In the latter equation, $a = \sqrt{\frac{\mu\Omega}{\hbar}}$ represents the inverse of the effective size of the dot, which is controlled by both the geometric size of the dot and the magnetic field. $L_n^{|m|}(a^2 r^2)$ indicates the associated Laguerre polynomial.

The mathematical form of $\mathcal{H}^{\rm cm}$ is given by:

$$\mathcal{H}^{\rm cm} = \frac{P_R^2}{2M_0} + \frac{1}{2}M_0\Omega^2R^2 - \frac{1}{2}\omega_c L_Z + \mathcal{H}_z^0, \tag{10}$$

here $M_0 = 2m_{hh}$, L_Z is the angular momentum associated with CM. The Zeeman term of Hamiltonian can be expressed as ($\mathcal{H}_z^0 = \frac{M_0\hbar\omega_c g^* S}{4m_0}\sigma_z$), where $S = 5/2$.

Let us define an effective unit for length as $a^* = \frac{\varepsilon_\infty \hbar^2}{\mu e^2}$ in the relative donor unit framework and the corresponding one for energy as $R^* = \frac{\hbar^2}{2\mu a^{*2}}$ [54]. The effective units for CM can be defined analogously to their counterparts for $\mathcal{H}_{\rm rel}^0$ but with total mass M_0 instead of the reduced mass μ. This leads to rescaling expression for a^*, yet the expression for R^* remains the same. Consequently, in the absence of the Coulomb potential and the polaronic contributions, the energies of the non-interacting holes refer to energies of relative and CM parts: [45]

$$E_{n,m}^{\rm rel(0)} = 2\gamma_1\left(2n + |m| + 1\right) - m\gamma_2. \tag{11}$$

$$E_{N,M}^{\rm cm} = 2\gamma_1\left(2N + |M| + 1\right) - M\gamma_2 + \frac{g^* S M_0\gamma_2}{2m_0}, \tag{12}$$

where $\gamma_1 = \frac{\hbar\Omega}{2R^*}$ and $\gamma_2 = \frac{\hbar\omega_c}{2R^*}$. The indices m and M can both take the values $0, \pm1, \pm2\ldots$

By considering the Coulomb potential and hole–LO–phonon coupling, the energy of the relative part can be calculated by computing the total energy expression:

$$E_{n,m}^{\rm rel} = 2\gamma_1\left(2n + |m| + 1\right) - m\gamma_2 + \left\langle f_{n,m}(r)\left|V^{int}(r)\right|f_{n',m'}(r)\right\rangle, \tag{13}$$

where the mean value of the hole–hole interaction and hole–LO–phonon interaction is obtained by determining the matrix elements:

$$\left\langle \Psi_{n,m}\left|V^{\rm int}(r)\right|\Psi_{n',m'}\right\rangle = \int_0^\infty f_{n,m}^*(r)\,V^{\rm int}(r)\,f_{n',m'}(r)\,\delta_{nn'}\delta_{mm'}r{\rm d}r, \tag{14}$$

where $\delta_{nn'}$ and $\delta_{mm'}$ are the Kronecker delta symbols.

The calculated wave functions and energy spectra allow direct evaluation of the magnetotransport and magnetocaloric characteristics of (Ga,Mn)As-based quantum dots. By adopting the canonical ensemble of Boltzmann–Gibbs statistics, these functions are derived from the partition function

$$Z_c = \sum_i \exp\left(-\beta E_i\right), \tag{15}$$

with $\beta = (k_{\rm B}\mathcal{T})^{-1}$; $k_{\rm B}$ and $\mathcal{T}$ are the Boltzmann constant and absolute temperature, respectively. In this approach, the main thermodynamic properties of the system can be deduced using Z_c.

The heat capacity defines the quantity of energy storage:

$$C_v = -k_{\rm B}\beta^2\left(\frac{\partial\langle E\rangle}{\partial\beta}\right), \tag{16}$$

where $\langle E\rangle$ is the mean energy of the system.

The entropy, is one of the most essential thermodynamic properties, describes the randomness of the system. It can be obtained through the relation:

$$S = k_{\rm B}\beta\left(\langle E\rangle - F_{\rm H}\right), \tag{17}$$

where $F_{\rm H} = F = -k_{\rm B}\mathcal{T}\ln Z_c$ is the Helmholtz free energy describing the stability criterion.

The magnetization $\mathcal{M}$ can be extracted from the statistical relation [55]:

$$\mathcal{M} = \frac{-1}{Z_c}\sum_i \frac{\partial E_i}{\partial B}\exp\left(-\beta E_i\right). \tag{18}$$

We also recall that the magnetic susceptibility

$$\chi = \frac{\partial\mathcal{M}}{\partial B}, \tag{19}$$

determines the degree of magnetization of a given material submitted to a magnetic field (B) [56].

Magnetocaloric effect (MCE) is the response of the magnetic moments of a magnetic material to the action of an external magnetic field at a particular temperature. Under the influence of a varying magnetic field, the MCE provides information about the change in temperature, or exchange heat, in a magnetic material with a thermal reservoir. The magnetocaloric entropy change (ΔS_{M}) and adiabatic temperature change ($\Delta \mathcal{T}_{\mathrm{ad}}$) are the critical parameters to characterize the magnetocaloric behavior of the material. In an isothermal process, ΔS_{M} can be obtained by the difference between the entropy with magnetic field $S(\mathcal{T}, B)$ and entropy without magnetic field $S(\mathcal{T}, B = 0)$. It is given by [57]:

$$\Delta S_{\mathrm{M}}(\mathcal{T}, B) = S(\mathcal{T}, B \neq 0) - S(\mathcal{T}, B = 0). \tag{20}$$

In these conditions, the adiabatic temperature change $\Delta \mathcal{T}_{\mathrm{ad}}$ can be extracted through the relation:

$$\Delta \mathcal{T}_{\mathrm{ad}}(\mathcal{T}, B) = -\mathcal{T}\frac{\Delta S_{\mathrm{M}}(\mathcal{T}, B)}{C_v(\mathcal{T}, B)}. \tag{21}$$

In a semiclassical picture, the circular motion of a hole implies that there is an azimuthal current. The corresponding quantum-mechanical current density $\overrightarrow{j}_{n,m}$ carried by the definite orbital with quantum numbers n and m can be obtained from: [58, 59]

$$\overrightarrow{j}_{n,m} = -\left[\frac{e\hbar}{m^*_{hh}}\Im\left(\Psi^*\nabla\Psi\right) + \frac{\mathrm{e}^2}{m^*_{hh}}\overrightarrow{A}\Psi^*\Psi\right]. \tag{22}$$

By integrating this expression over the radial axis, one can calculate the current J carried by the state with quantum numbers n, m. The result is given as

$$J_{n,m} = \int_0^\infty j_{n,m}(\rho)\,\mathrm{d}\rho, \tag{23}$$

where $\rho = \rho(r, R)$. The total persistent current is the sum of contributions from the CM motion J^{cm} and the contribution from the relative motion J^{rel}:

$$J = J^{\mathrm{CM}} + J^{\mathrm{rel}}. \tag{24}$$

For the CM, the problem is identical to the case of a single-hole system; therefore, the current density calculation based on equation (23) gives the result

$$J^{\mathrm{CM}}_{N,M} = \int_0^\infty -\frac{1}{2\pi}\frac{e\hbar}{m^*_{hh}}\left[\frac{M}{R} + \frac{e}{\hbar}A(R)\right] f^2_{N,M}(R)\,\mathrm{d}R. \tag{25}$$

The current carried by the relative motion is obtained in the usual manner with the use of equation (23)

$$J^{\mathrm{rel}}_{n,m} = -\frac{e\omega_0}{2\pi}\left(1 + \frac{1}{4}\frac{\omega_c^2}{\omega_0^2}\right)^{\frac{1}{2}} m \sum_{n,n'=0}^{\infty}\left(\frac{n!}{(n+|m|)!}\frac{n'!}{(n'+|m|)!}\right)^{\frac{1}{2}} \int_0^\infty \mathrm{e}^{-r} r^{|m|-1} L_n^{|m|}(r)\, L_{n'}^{|m|}(r)\,\mathrm{d}r - \frac{e}{4\pi}\omega_c. \tag{26}$$

The persistent current I at finite temperature $\mathcal{T}$ is of principal interest and can be obtained by taking the ensemble average of $J^{\mathrm{CM}}_{N,M} + J^{\mathrm{rel}}_{n,m}$ over the canonical ensemble, whose explicit expression is given by

$$I = \frac{1}{Z_{\mathrm{CM}}}\sum_N\sum_M J^{\mathrm{CM}}_{N,M}\mathrm{e}^{-\beta E^{\mathrm{CM}}_{N,M}} + \frac{1}{Z_{\mathrm{rel}}}\sum_n\sum_m J^{\mathrm{rel}}_{n,m}\mathrm{e}^{-\beta E^{\mathrm{rel}}_{n,m}}. \tag{27}$$

3. Results and discussions

The numerical calculation of our formalism is applied essentially for (Ga, Mn)As with a high concentration of Mn where the material is to prone to have antiferromagnetic behavior. As described in the previous section, the energy of the system of two holes, $E = E^{\mathrm{cm}}_{N,M} + E^{\mathrm{rel}}_{n,m}$, incorporates the effect of hole–LO–phonon coupling strength which enters the $E^{\mathrm{rel}}_{n,m}$ expression.

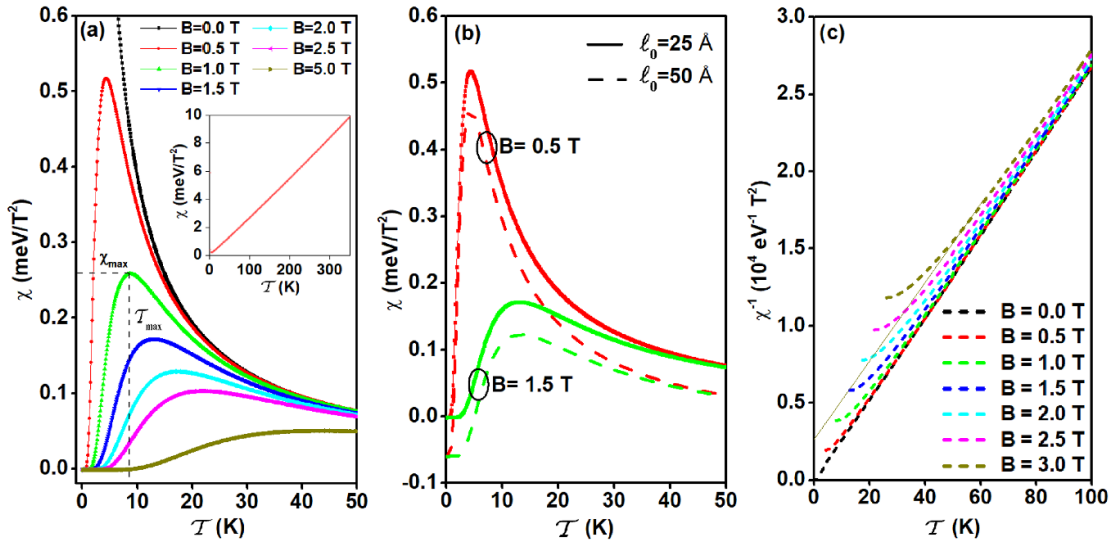


Figure 2. Presents the temperature evolution of the magnetic susceptibility for several magnetic field strengths at $l_0 = 25$ Å. It also compares susceptibility behaviors corresponding to strong ($l_0 = 25$ Å) and weak ($l_0 = 50$ Å) confinement regimes. In addition, the temperature dependence of the inverse susceptibility is shown for the strong confinement case.

Table 2. Curie constant (C) and Weiss paramagnetic temperature (θ).

B (T)	0	0.5	1	1.5	2	2.5	5
C (meV T^{-2} K)	3.3064	3.3067	3.3074	3.3088	3.3106	3.3131	3.3334
$\theta = -T_C$ (K)	23.46	23.40	23.23	22.94	22.52	21.98	17.45

The confinement strength is quantified using the characteristic length $l_0 = \sqrt{\hbar/(m^*_{hh}\omega_0)}$ associated with the harmonic potential, where m^*_{hh} is the effective heavy-hole mass. Two limiting regimes are considered: strong confinement with $l_0 = 25$ Å ($\hbar\omega_0 = 23.9$ meV) and weak confinement with $l_0 = 50$ Å ($\hbar\omega_0 = 6$ meV). The former satisfies $l_0 \leqslant a^*$, while the latter corresponds to $l_0 > a^*$, where a^* is the effective Bohr radius.

According to equation (18), the quantity $\mathcal{M}$ describes how the system responds magnetically to an external field and its temperature dependence is frequently linked to structural phase transitions.

Figure 2(a) displays the temperature dependence of magnetic susceptibility (χ) curve in the applied magnetic field range from 0 to 5 T. The first observation that we can make here is that at $B = 0$ T, $\chi(\mathcal{T})$ varies according to the power law $\mathcal{T}^{-\alpha}$, with a fit parameter $\alpha \simeq 1$. At $B \neq 0$ T, $\chi(\mathcal{T})$ changes its behavior and exhibits a maximum $\chi_{\max}(\mathcal{T})$ at specific temperature $\mathcal{T}_{\max}$. Beyond this temperature, the system loses its susceptibility and enters a magnetization-saturation regime. Our calculation shows that the maximum susceptibility decreases in intensity and shifts to higher $\mathcal{T}$ with increasing magnetic field. In the absence of a magnetic field, the magnetic moments in a paramagnetic material are disordered due to thermal agitation. There is no preferred spin orientation and therefore no macroscopic magnetization. In addition, the material remains globally unmagnetized (magnetization $\mathcal{M} = 0$). But according to Curie's law, the magnetic susceptibility $\chi = C/\mathcal{T}$ remains well defined, even without a field. This means that: the material is ready to magnetize as soon as a field is applied and at low temperature, the easier it would be to induce magnetization if a field were present.

In order to analyze the influence of the degree of confinement on the susceptibility, we plot in figure 2(b) the variation of $\chi(\mathcal{T})$ for two confinement strengths $l_0 = 25$ Å and $l_0 = 50$ Å and for two values of magnetic field ($B = 0.5$ and 1.5 T). Our calculation shows that the magnetic susceptibility is more pronounced in strong confinement ($l_0 = 25$ Å). The maxima occur at approximately the same critical temperature, independent of the degree of confinement. However, there is a qualitative difference between the systems with strong and weak confinement: the susceptibility is always positive for the former, but changes sign as $\mathcal{T} \to 0$, a signature of diamagnetic behavior.

To complete the understanding of the magnetic property of the system, we plot the inverse of the magnetic susceptibility $\chi^{-1}(\mathcal{T})$ in figure 2(c), corresponding to the temperature $\mathcal{T} > \mathcal{T}_{\max}$ regime. This figure demonstrates that $\chi^{-1}(\mathcal{T})$ exhibits a linear behavior above a certain temperature, as described by

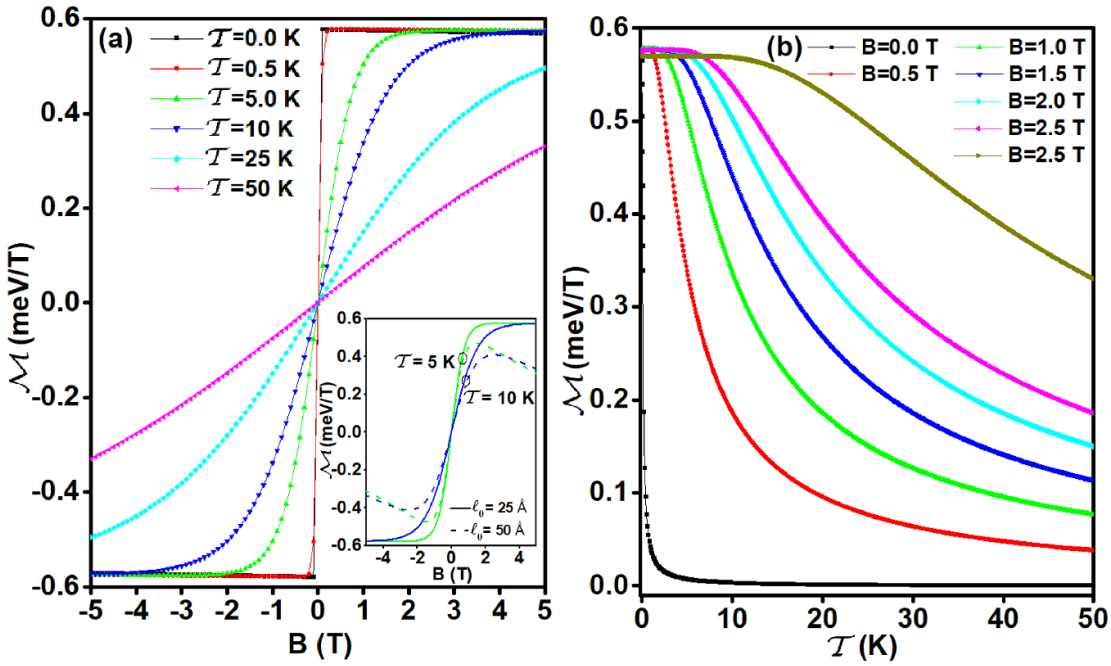


Figure 3. (a) Magnetic field dependence of magnetization at different values of temperature for $l_0 = 25$ Å. Inset shows comparison between the temperature dependence of magnetization in the cases of strong confinement $l_0 = 25$ Å (solid lines) and weak confinement $l_0 = 50$ Å (dashed lines). (b) Temperature dependence of magnetization at different values of the magnetic field for $l_0 = 25$ Å.

the Curie–Weiss law

$$\chi = C/(\mathcal{T} + \theta), \tag{28}$$

where $C = \frac{N\mu_{\text{eff}}^2}{3K_B}$ is known as Curie constant and θ is the Weiss paramagnetic temperature [66]. The fit of $\chi^{-1}(\mathcal{T})$ allows us to derive the values for θ and C. The single thin solid line in the figure is provided as an example of the extrapolation of the linear fit down to zero temperature. The point of crossing between the fit and the vertical axis occurs at a positive value, $\chi^{-1}(\mathcal{T} = 0) = \theta/C > 0$, which can be visually confirmed to be the same for all the other lines (i.e. other values of magnetic field). The fitted parameters are shown in table 2. The observed positive values of θ (corresponding to the negative values of T_C reveal that, for sufficiently high temperature, antiferromagnetic hole–hole interactions are associated with ferromagnetic ordering in GaMnAs, which is in agreement with some previous studies [67–70]. We consider this as the main finding of the present work. The maximum in the curve of magnetic susceptibility as a function of temperature observed can be explained by a transition between two magnetic regimes: at low temperatures, the antiferromagnetic order begins to be thermally disturbed. The material becomes more reactive to a magnetic field, increasing its susceptibility. The susceptibility reaches a maximum near the Néel temperature T_N. Above T_N, antiferromagnetic order disappears and Curie–Weiss behavior is observed [71]. Strong confinement enhances antiferromagnetic coupling, whereas weak confinement increases hole mobility and leads to a diamagnetic-like response.

At this point, let us discuss the sample's magnetization behavior. Figure 3(a) represents the B-dependence of the magnetization $\mathcal{M}(B)$ in (Ga,Mn)As, for various values of temperature (from $\mathcal{T} = 0$ K to $\mathcal{T} = 50$ K) for $l_0 = 25$ Å. The curves of magnetization rise rapidly at low magnetic fields and then saturate as the field increases. To study magnetic reversibility, magnetization curves were measured in field-increase and field-decrease modes for $B(\text{T}) = [-5, +5]$. In conclusion, there is no magnetic hysteresis, which indicates that the magnetic transitions are perfectly reversible. The inset of figure 3(a) shows that, the same behavior is observed for both types of confinement ($l_0 = 25$ Å and $l_0 = 50$ Å) and two values of temperature ($\mathcal{T} = 5$ K and $\mathcal{T} = 10$ K) for small intensities of magnetic field. We note that, similar to the magnetic susceptibility, the magnetization is also more pronounced for the case of strong confinement. However, for a sufficiently strong magnetic field, the behavior of magnetization diverges for the two cases, and we can observe a decrease in $|\mathcal{M}|$ for an increase in $|B|$ for the weak confinement. This behavior under a sufficiently strong magnetic field is also a signature of diamagnetism in the weak confinement case, as was pointed out previously in the case of negative χ at $\mathcal{T} \to 0$.

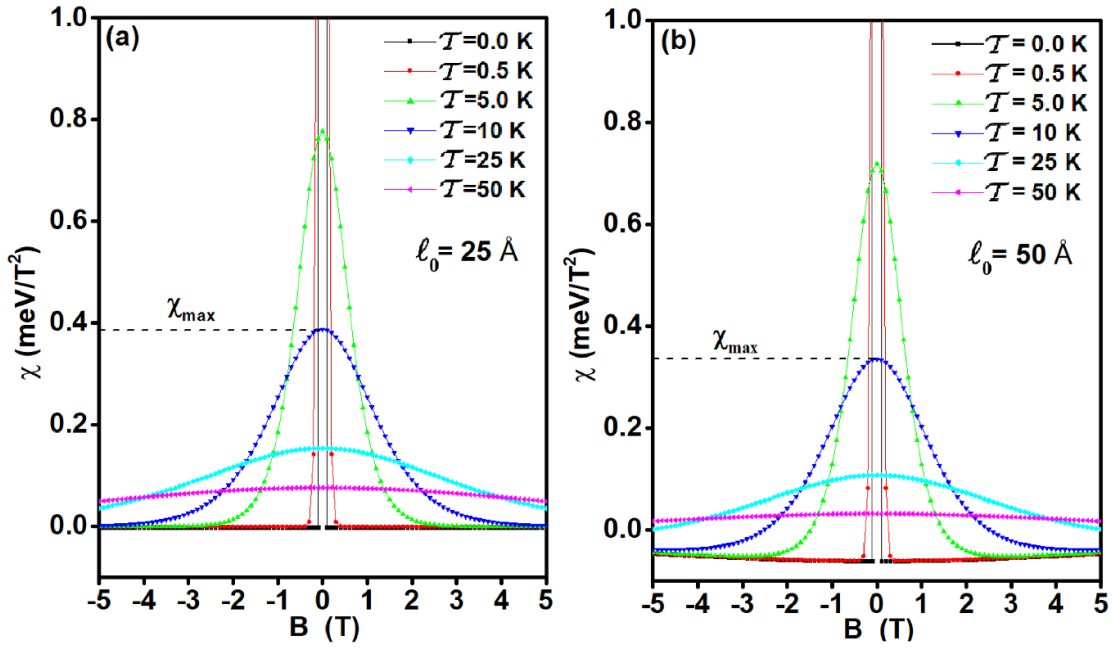


Figure 4. Magnetic field dependence of magnetic susceptibility at different values of temperature: (a) for $l_0 = 25$ Å, (b) for $l_0 = 50$ Å.

To better understand the system's dependence on temperature, we have plotted magnetization vs. $\mathcal{T}$ for magnetic field strengths $0-5$ T in the range shown in figure 3(b). At low temperatures, the magnetization is maximal, while it gradually decreases with increasing temperature, leading to the appearance of paramagnetic order. These results are in perfect agreement with the principles of the Curie–Weiss law. However, at a given temperature, as the magnetic field strength increases, the magnetization gradually aligns with the field, as noted earlier.

Figure 4(a) represents the variation of magnetic susceptibility χ in (Ga, Mn)As as a function of the magnetic field strength for different low temperatures, ranging from 0 to 50 K, for $l_0 = 25$ Å. For all temperatures considered, the magnetic susceptibility has a single maximum at $B = 0$ and diminishes symmetrically with $|B|$ of either sign. Moreover, the susceptibility peaks maxima decrease as the temperature increases. As we can see from the figure, the curves of χ decrease rapidly at a weak magnetic field and then tend to zero as the field increases, which reflects the saturation of the antiferromagnetic order. Figure 4(b) represents the variation of χ in the case of $l_0 = 50$ Å. The behavior is, in general terms, similar to that observed in figure 4(a), except that the susceptibility curves are less pronounced than shown in the previous figure. One important difference is that, in the case of $l_0 = 50$ Å, for $\mathcal{T} < 25$ K the susceptibility always becomes negative for sufficiently strong $|B|$. Again, this means that strong magnetic fields and low temperatures favor diamagnetic behavior in the case of weak confinement. This negative susceptibility is completely absent in the strong confinement system.

Figure 5 presents the magnetic susceptibility in (Ga, Mn)As as function of temperature for two fixed parabolic confinement potentials $l_0 = 25$ Å (figure 5(a)) and $l_0 = 50$ Å (figure 5(b)), at $B = 1.5$ T and investigates the impact of hole–LO–phonon coupling. It can be observed in the figure that, for a given B, the presence of hole-LO-phonon interactions (black line) enhances the system's susceptibility. The polaron effect due to hole–LO phonon coupling is stronger in weakly confined systems ($l_0 = 50$ Å) than in strongly confined ones ($l_0 = 25$ Å). While in the latter one, including the hole-phonon interaction results only in a minimal quantitative reinforcement of susceptibility, in the former case it enables or disables the diamagnetic-like response (negative susceptibility) as $\mathcal{T} \to 0$ for the particular value of $B = 1.5$ T shown in figure 5(b). Figure 5 illustrates the interplay between phonon coupling and diamagnetic behavior, highlighting that the absence of phonons tends to favor diamagnetic behavior in systems with weak confinement. Phonons, which are quantized vibrations of the crystal lattice, can interact with the material's magnetic moments, either disrupting or enhancing their alignment with an external magnetic field. When phonon coupling is strong, these lattice vibrations can reduce the coherence of magnetic alignment, often leading to behaviors like paramagnetism or antiferromagnetism. However, when phonons are absent or weakly coupled, there is less disruption of the spins, allowing them to align more freely with the external field. In the case of weak confinement, the lack of phonon interactions promotes

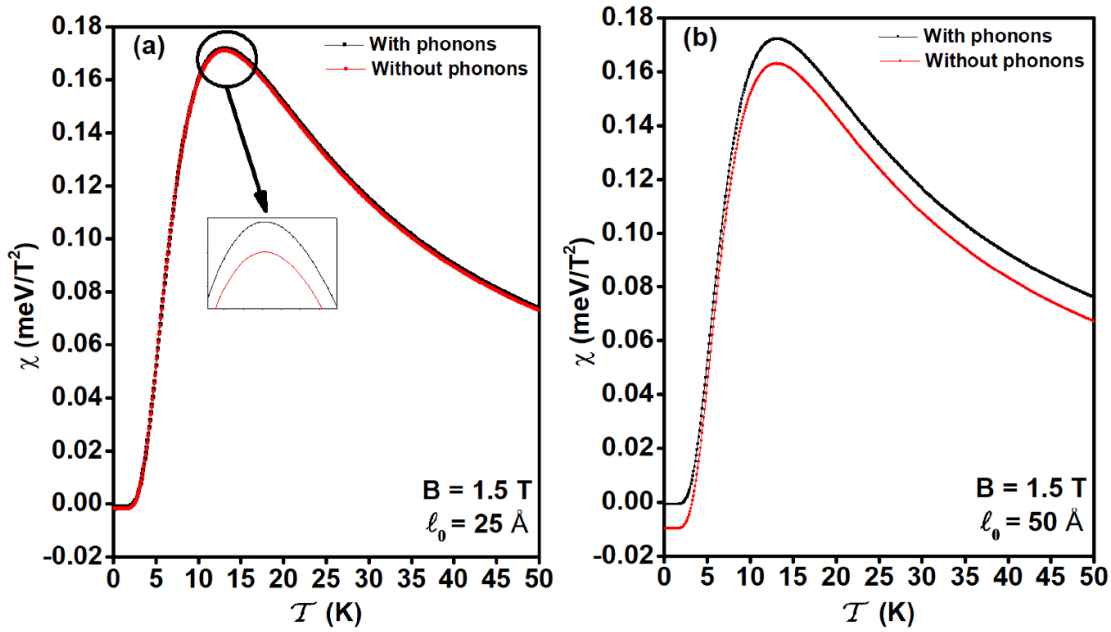


Figure 5. Temperature dependence of the magnetic susceptibility under strong (a) and weak (b) confinement regimes. Black and red curves represent calculations performed with and without phonon contributions, respectively.

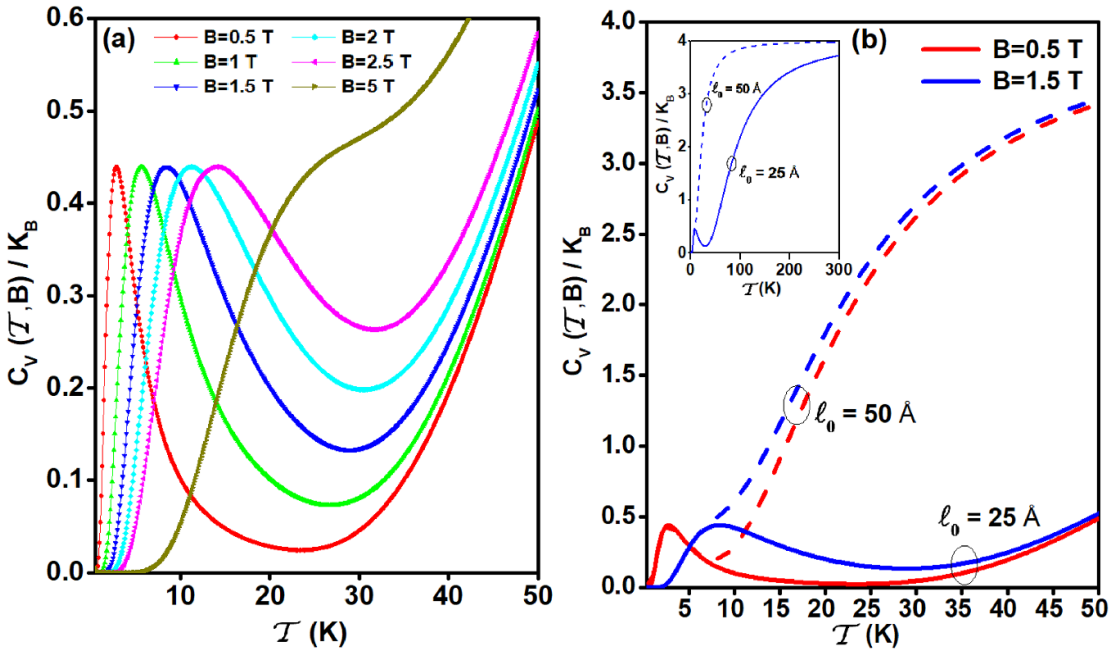


Figure 6. Temperature-dependent heat capacity, (a) in the range of magnetic field intensities from $B = 0.5$ to $B = 5$ T for $l_0 = 25$ Å , and (b) the contrast between strong and weak confinement characterized by ($l_0 = 25$ Å) and ($l_0 = 50$ Å), respectively.

a diamagnetic response, in which the material generates a small opposing magnetic moment that repels the field rather than aligning with it. Essentially, the absence of phonons means the spins are less influenced by lattice vibrations, and the system exhibits a weaker, diamagnetic response instead of a stronger alignment with the field, a behavior that is more pronounced under weak confinement conditions.

Let us now discuss the thermodynamic properties of the system taking heat capacity C_V into account. The heat capacity defines the quantity of energy storage. Figure 6(a) displays the variation of this quantity as a function of temperature for various magnetic field values ($B \in \{0.5, 1, 1.5, 2, 2.5, 5\}$ T) for the strong confinement $l_0 = 25$ Å. The first remark is that a peak is observed in the heat capacity curves, corresponding to the well-known Schottky anomaly, often observed in low-dimensional materials. However, an applied magnetic field between 0.5 T and 5 T imposes Zeeman splitting on the spin system,

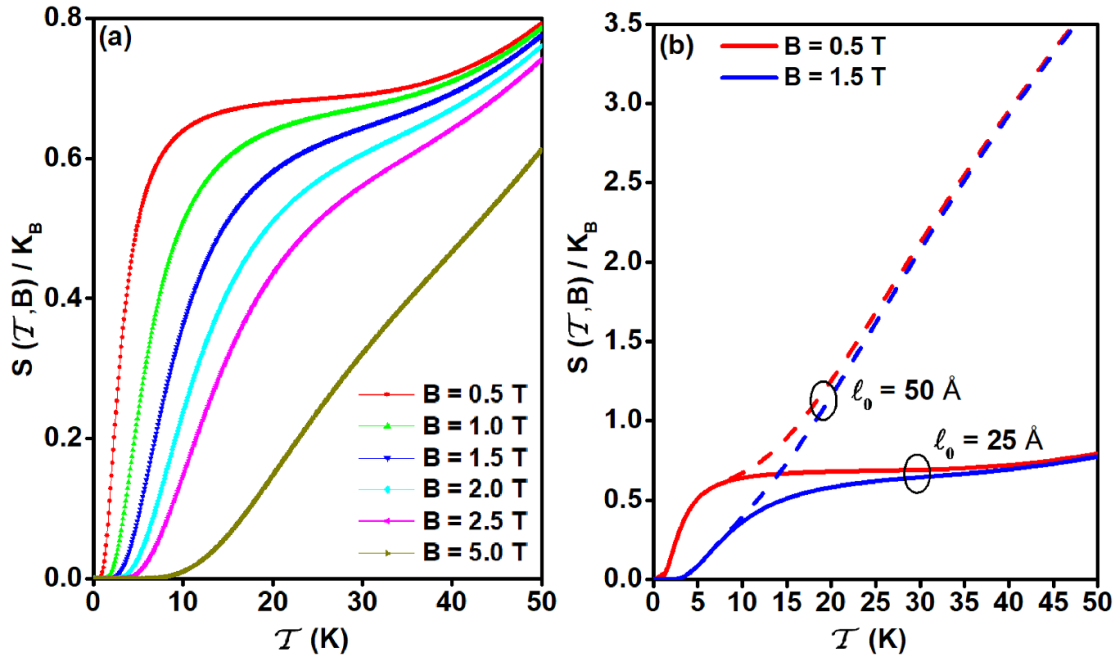


Figure 7. Entropy as a function of temperature, (a) for $l_0 = 25$ Å in the range of magnetic field intensities from $B = 0.5$ T to $B = 5$ T, (b) comparison between the strong ($l_0 = 25$ Å) and weak ($l_0 = 50$ Å) confinement cases.

with its magnitude increasing with the field strength. The specific heat anomaly can be shifted toward a selected temperature. The heat-capacity peak arises from energy absorption during the phase transition, and an applied magnetic field broadens it by spreading magnetic-moment randomization over a wider temperature range [57].

Figure 6(b), compares the change of heat capacity for (Ga,Mn)As as function of temperature for two confinement strengths: $l_0 = 25$ Å ($\hbar\omega_0 = 23.9$ meV), shown with the solid lines, and $l_0 = 50$ Å ($\hbar\omega_0 = 6$ meV), marked with the dashed lines, and for two values of the magnetic field ($B = 0.5$ T—red lines—and $B = 1.5$ T—black lines).

Two distinct temperature regimes are clearly visible in the behavior of C_v. For sufficiently small temperatures, both red lines are indistinguishable, and so are the black lines. However, the red lines are quantitatively separated from the black lines. It is worth noting that, for low temperatures, the heat capacity for both values of magnetic field strength has the same qualitative behavior, exhibiting a single peak, but there is a qualitative difference, namely, under stronger magnetic fields $B = 1.5$ T (black), the peak is both shifted towards higher temperatures and broadened. This was previously discussed for figure 6(a) for $l_0 = 25$ Å, and figure 6(b) confirms that this is confinement-independent. Finally, we can conclude that the magnetic field is the quantity tuning qualitatively the heat capacity in the low temperature regime and the confinement strength is almost irrelevant.

On the other hand, the high-temperature picture is the opposite. In this case, both dashed lines converge, and so do the solid ones, pointing to the lack of relevant impact of the magnetic field. Conversely, the behavior exhibited by two different line styles (dashed vs solid) trends is visibly different, marking the confinement strength as the dominant factor in the high temperature regime. In order to determine if this difference between $l_0 = 25$ Å and $l_0 = 50$ Å systems is a qualitative or a quantitative one, the results for temperature up to 300 K and $B = 1.5$ T are shown in the inset. The capacity shows saturation at the same level, irrespective of confinement, although at a visibly slower rate in the strong-confinement case, allowing us to interpret the difference in the strength of the confinement as a simple rescaling of the temperature parameter of the heat capacity trend in the high-temperature regime.

There is an additional qualitative difference, visible in the C_v behavior for the intermediate values of $\mathcal{T}$, situated between the low temperature and the high temperature limits described previously. In this case, a direct interplay between the magnetic field and temperature is observed, rather than one quantity dominating the behavior. The curves corresponding to $l_0 = 25$ Å (solid) exhibit a minimum centered at around 30–33 K and then start increasing again. This peak-minimum-increase curve is also exhibited by the dashed red line ($l_0 = 50$ Å confinement under 0.5 T) but not the dashed black one (for $B = 0.5$ T). In the latter case, the curve follows the low-temperature trend until the middle of the peak, then the

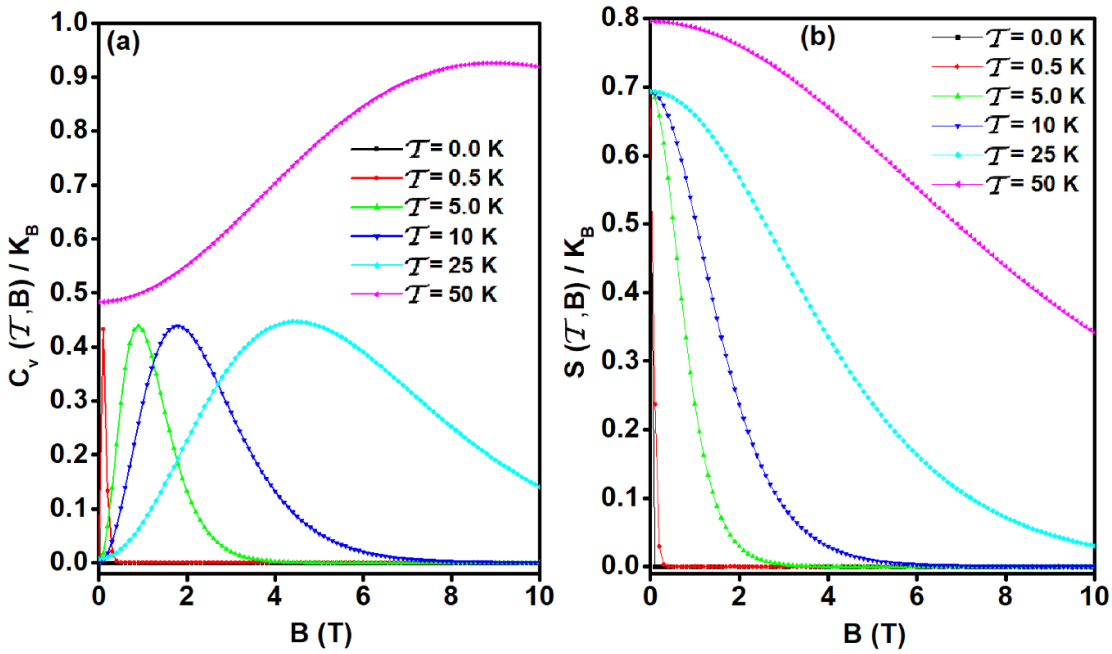


Figure 8. Heat capacity (a) and entropy (b) as functions of magnetic field, for various values of temperature ($\mathcal{T} \in \{0, 0.5, 5, 10, 25, 50\}$ K) in the strong confinement $l_0 = 25$ Å case.

increase toward saturation characteristic of the high-temperature regime begins immediately. In this case, there is no minimum corresponding to the intermediate values of temperature.

The heat capacity is also directly dependent on the system's magnetic entropy

$$S(\mathcal{T},B) = \int \frac{C_V}{\mathcal{T}} \mathrm{d}\mathcal{T}, \tag{29}$$

which defines the disorder and the system's randomness. Currently, magnetic entropy is under extensive investigation for potential spintronics applications. The figure 7(a), illustrates the change of entropy in (Ga,Mn)As with temperature for various magnetic field values ($B \in \{0.5, 1, 1.5, 2, 2.5, 5\}$ T) for the strongly confined system $l_0 = 25$ Å. We note that at zero temperature, the system's entropy is zero; it increases with increasing temperature, due to the system's greater randomness as thermal energy increases. Additionally, we observe that entropy decreases as the magnetic field intensity increases (from 0.5 to 5 T). The origin of this behavior is easy to understand from the character of the C_V curves in 7(a) in conjunction with the relation equation (29). One thing to note is that the $S(\mathcal{T},B)$ curve is always monotonic in $\mathcal{T}$ as opposed to the $C_V(\mathcal{T},B)$ one. Figure 7(b) shows the temperature dependence of entropy in (Ga,Mn)As for confinement lengths $l_0 = 25$ Å and $l_0 = 50$ Å under magnetic fields of 0.5 T and 1.5 T. In this case, we can observe two distinct temperature regimes in the results. In the case of small $\mathcal{T}$, the magnetic field is the dominant quantity (both red lines overlap, as well as both black ones), and in the high temperature regime, the dependence of entropy on the temperature is decided by the confinement instead. This is analogous to what was previously observed for the heat capacity dependence in figure 6(b). The one difference is that, in the present case of entropy in figure 7(b), there is no minimum in the intermediate range of temperatures and the transition between the low and high temperature regimes is straightforward, which also translates into the absence of any qualitative effects of the $\mathcal{T} - B$ interplay.

In figure 8(a), we present the heat capacity of an interacting two-hole system as a function of B for several values of $\mathcal{T}$. At $\mathcal{T} = 0$ K, the heat capacity is null for all B values, resulting from the 3rd law of thermodynamics. For $\mathcal{T} \neq 0$ K, C_V exhibits a single maximum e.g. around 0.1 T for 0.5 K. This anomaly peak shifts to higher B and broadens as the temperature increases. In all cases, the specific heat seems to cancel out at a sufficiently high B [72]. The Schottky anomaly observed in the specific heat curves is a characteristic feature of systems with a bounded discrete energy spectrum and does not depend on the dimensionality of the system. In systems with a finite energy-level spacing, the anomaly occurs at the temperature corresponding to the inflection point of the internal energy as a function of temperature. The observed shift of the anomaly towards higher temperatures with increasing magnetic field arises from the widening of the energy-level spacing due to Zeeman splitting. To better understand the

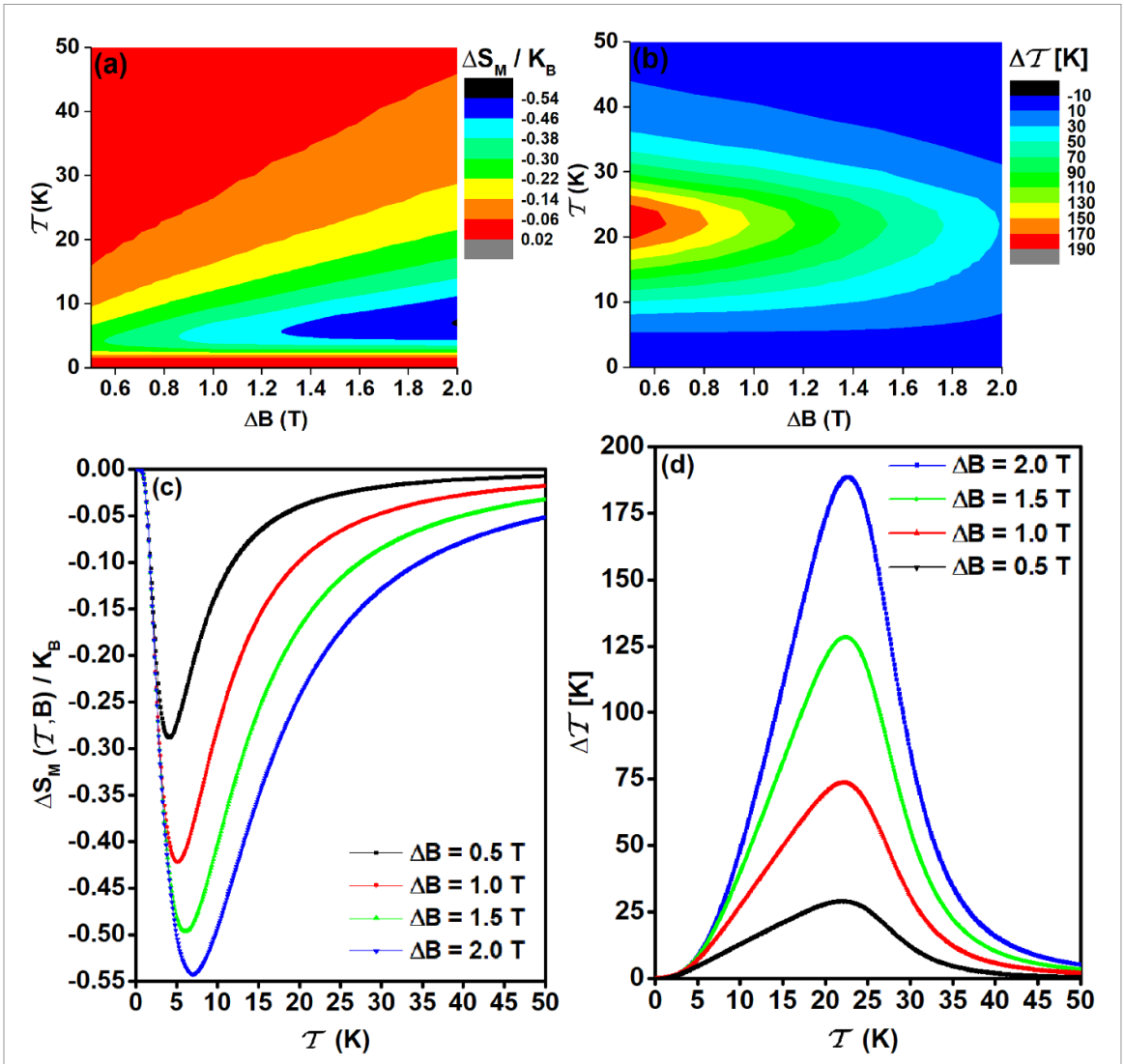


Figure 9. variation of ΔS_{M} and $\Delta \mathcal{T}_{\mathrm{ad}}$, with temperature, along the $\Delta B \in \{0.5, 1, 1.5, 2\}$ T .

confinement effect of the magnetic force, we have plotted figure 8(b), which displays the dependence of the entropy on the magnetic field in (Ga,Mn)As with several different values of temperature. The figure shows that B reduces the system's entropy, while temperature increases it. When $\mathcal{T} \to 0$, the temperature derivative of entropy becomes zero, as the laws of thermodynamics require. It is worth noting that the behavior of the both quantities in figures 8(a) and (b) in the $B \to 0$ limit is the same for all the $\mathcal{T}$ values shown, with the exception of the $\mathcal{T} = 50$ K one. This is because the latter value lies in the high temperature regime in opposite to all the other ones, which in contrast belong to the low temperature regime, as was described above; for comparison, let us recall that the minimum in C_V for the strong confinement system was localized at $30 - 33$ K, see figure 6(b).

As previously mentioned, the MCE magnitude can be described by ΔS_{M} and/or $\Delta \mathcal{T}_{\mathrm{ad}}$. The dependence of the magnetocaloric entropy change of the system with strong confinement on both the temperature and on the magnetic field is shown in figure 9(a) as a color map and the corresponding characterization of the adiabatic temperature change is given by figure 9(b). Additionally, the sections of the maps for several constant values of B, are provided in figure 9(c) in the case of ΔS_{M} and in figure 9(d) for $\Delta \mathcal{T}_{\mathrm{ad}}$.

As shown in the figures 9(a) and (c), the maximum magnitude of the magnetocaloric entropy change for $\Delta B = 0.5$ T is $|\frac{\Delta S_{\mathrm{M}}}{K_{\mathrm{B}}}| = 0.29$. As the applied magnetic field increases, the maximum magnitude increases linearly up to 0.54 for a field intensity of 2 T, while the corresponding negative peak shifts to higher temperatures and broadens.

The adiabatic temperature change ($\Delta \mathcal{T}_{\mathrm{ad}}$) is a vital quantity in the analysis of magnetic refrigeration. In the present work, the $\Delta \mathcal{T}_{\mathrm{ad}}$ was estimated with the help of equation (21). Figures 9(b) and (d) illustrate the temperature dependence of $\Delta \mathcal{T}_{\mathrm{ad}}$ for several magnetic field intensities. $\Delta \mathcal{T}_{\mathrm{ad}}$ reaches

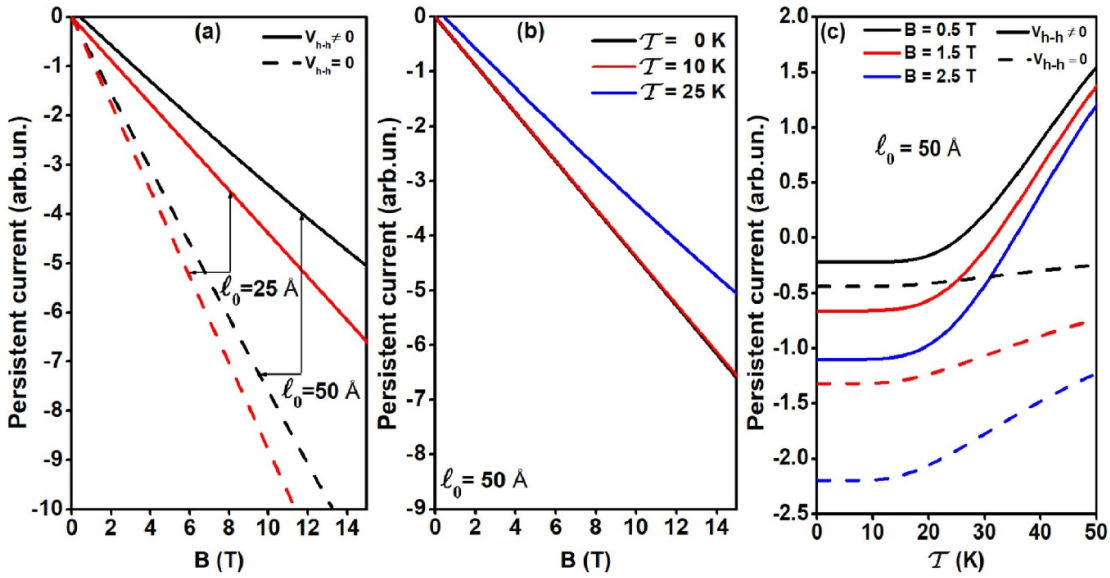


Figure 10. (a) Persistent currents I vs. B at zero temperature for both strong confinement $l_0 = 25$ Å (red lines) and weak confinement $l_0 = 50$ Å (black lines) cases. (b) Persistent currents I vs. B at finite temperature for $l_0 = 50$ Å. (c) Persistent currents vs. temperature for $B = 0.5$, $B = 1.5$, and $B = 2.5$ T, at $l_0 = 50$ Å. (a) and (c) show the effect of the hole–hole interactions.

a maximum value of 30 K for $B = 0.5$ T; the value of this maximum rises as the applied magnetic field increases and attains 178 K for $B = 2$ T. The position of the $\Delta\mathcal{T}_{\rm ad}$ peak shifts towards higher $\mathcal{T}$ and broadens for increasing B, as it was happening in the case of $\Delta S_{\rm M}$. This strong change of the temperature dependence of the MCE quantities on the magnetic field suggests that (Ga,Mn)As is a good candidate for spintronic applications.

Here, we will discuss the persistent currents in the system. We recall that the calculation of the persistent currents is similar to that of the eigenvalues of the relative energy calculation. First, let us discuss the impact for hole–hole interaction. In this case, the persistent current I was obtained from the values of $J^{\rm c.m}$ and $J^{\rm rel}$ for the ground state, characterized by $N = M = n = m = 0$ quantum numbers at zero temperature. The results for both the strong and the weak confinement are shown in figure 10(a), where the dependence of the current I on the magnetic field is presented. It can be observed that I has a negative sign for $\mathcal{T} = 0$ and it decreases linearly in value, or equivalently increases in magnitude, with increasing B in all cases. The presence of the Coulomb interaction decreases the current, while strong confinement increases it. However, the effect of the interaction (solid vs dashed lines) is visibly relatively stronger than the difference between the two confinement strengths (black vs red lines). Moreover, the impact of the interactions, as well as the one difference between the two confinements, increases for stronger magnetic fields.

Additionally, in order to study the impact of the temperature on I, we present figure 10(b), which shows the dependence of the current on the magnetic field intensity for a few values of temperature ($\mathcal{T} = 0, \mathcal{T} = 10$ and $\mathcal{T} = 25$ K). We can see that the largest current–magnitude temperature was found in the low-temperature regime. It is worth mentioning that, while the current curve in the $B \in [0, 15]$ T interval almost does not change from zero temperature up to $\mathcal{T} = 10$ T, the change from $\mathcal{T} = 10$ T to $\mathcal{T} = 25$ T is quite pronounced.

This result can be followed more closely in figure 10(c), which displays the the persistent current in the $l_0 = 50$ Å system as a function of temperature for a few chosen values of the magnetic field. Both the interacting (solid lines) and non-interacting (dashed lines) cases are shown. Firstly, in all cases, we can discern two distinct regimes in the temperature dependence of the persistent current. In the low-temperature regime, the current is almost unaffected by temperature, resulting in an approximately flat curve. In this region, the current remains close to $I(\mathcal{T} = 0, B)$, which significantly depends on both magnetic field intensity and on whether the hole–hole interaction is taken into consideration or not. All currents have a negative sign, and their magnitude increases with increasing B. Additionally, this magnitude is larger in the system without the hole–hole interaction, which is in agreement with the previously discussed $\mathcal{T} = 0$ results of figure 10(a).

In the high-temperature regime, the persistent currents in the system also increase approximately linearly with magnetic field. It is visible that all the solid lines slowly converge to a single behavior in the high temperature case, which is also true for all the dashed lines, although in the latter case, it happens

much more slowly. Also, the slope of the common trend of the solid lines is much steeper than that of the dashed lines, marking a much stronger high-temperature response of the persistent current due to the hole–hole interaction.

Since the signs of $I(\mathcal{T}=0,B)$ are negative, the increase of I value results initially in decreasing magnitude of the current $|I|$. In the case of the system of non-interacting holes (dashed lines), this behavior persists over the entire investigated temperature range ($\mathcal{T}\in[0,50]$ K). However, in the hole–hole interaction system (solid lines), the dependence of the persistent current on temperature is more complex. The magnitude decrease happens until $I=0$ is encountered in the case of each B value, at which point no persistent current flows at all. Further increase of the magnetic field intensity results in the reverse of the current, which now flows in the opposite direction. Consequently, at sufficiently high temperatures, the current magnitude decreases with B, an opposite dynamic to that of the low-temperature regime. It is not impossible that an analogous change will also occur in the system of non-interacting holes if the positive slope continues beyond the scope shown in figure 10(c), but even in that case, it would happen for incomparably higher temperatures.

4. Final remarks

In summary, magneto-transport and magnetocaloric properties of the confined double hole system in diluted semiconductor (Ga,Mn)As containing 3% Mn have been studied in detail. The obtained results show that both mentioned types of properties are influenced by the magnetic field, hole–LO–phonon interactions, hole–hole interactions, and the strength of confinement in different ways.

As the main result of this work, the antiferromagnetic character of the hole–hole system at sufficiently high temperatures was found from magnetization and susceptibility analyses, consistent with ferromagnetic order in GaMnAs and in agreement with previous works.

Signatures of a weak diamagnetic-like behavior were observed in the magnetization and susceptibility of the system with weak confinement (not present in the strong confinement case) at low temperatures and/or in strong magnetic fields.

In the temperature dependence of both the heat capacity and the entropy, two temperature regimes are evident: at small $\mathcal{T}$, the magnetic field determines the behavior of these thermodynamic quantities, while at high temperatures it is the strength of the confinement that is dominant.

Isothermal magnetic entropy change (ΔS_{M}) and adiabatic temperature change $\Delta\mathcal{T}_{\mathrm{ad}}$ have been plotted to describe the MCE amplitude. Their maximum of $|\Delta S_{\mathrm{M}}/K_{\mathrm{B}}|$ and $\Delta\mathcal{T}_{\mathrm{ad}}$ values are respectively 0.54 and 178 K, and they correspond to the highest considered magnetic field intensity of 2 T. At high temperatures, the specific heat should approach a constant value, reflecting the thermal occupation of all available energy states. In our model, we confirm that the asymptotic limit of the specific heat corresponds to $C_{\mathrm{V}}\to k_{\mathrm{B}}$ per degree of freedom, in agreement with theoretical expectations for a bounded two-level-like system at high temperature. Regarding the MCE, we emphasize that the entropy calculations presented here account only for the contribution from the interacting two-hole subsystem. In a real (Ga,Mn)As sample, however, the dominant contribution to the magnetic entropy arises from the localized Mn^{2+} spins, each carrying spin $\mathcal{S}=5/2$. Therefore, the values of magnetocaloric entropy change (ΔS_{M}) and adiabatic temperature change $\Delta\mathcal{T}_{\mathrm{ad}}$ computed in this work do not represent the full macroscopic MCE properties of the material. A comprehensive evaluation of the MCE would require incorporating the Mn spin subsystem and its interaction with the hole states. This will be pursued in future work using a mean-field approach or Brillouin-function modeling of the Mn spin ensemble. The calculation of the persistent currents of the two quantum dot holes has been performed both with and without Coulombic interaction. At very low temperatures, the current is not influenced by Coulomb interactions for the several small magnetic fields considered. The hole interaction is shown to be essential, especially in stronger magnetic fields. The reverse of the persistent current sign with increasing temperature, and the corresponding reverse in the ordering of the current magnitudes vs B from the low temperature regime to the high temperature regime, was found in the strongly confined system, as opposed to the weaker confinement case.

Regarding the future development of the present work, two avenues can be sketched here. Firstly, the confining potential adopted in our study was the two-dimensional parabolic one, which is in fact of the same kind as the one imposed by the external uniform magnetic field. The generalization of this study to different shapes of the quantum dot potential (e.g. the spherical one or rectangular ones), can bring into focus effects coming from interplay between confinements of different characteristics. Additionally, the hole is described in this work with the single heavy-hole band model. The generalization of this model to the multi-band $\vec{k}\cdot\vec{p}$ approach would be useful, in order to study the band-mixing effects on the magnetic, thermodynamic, and MCE properties of the double hole system.

Acknowledgments

LMP acknowledges financial support from Centers of Excellence with BASAL/ANID financing, CIA250002, CEDENNA. LMP and DL acknowledge partial financial support from ANID through FONDECYT 1240985. VC, WJP, and AEF acknowledge the grant from Project AS70, and the Chair 'Multiphysics and HPC' is led by Mohammed VI Polytechnic University and sponsored by OCP.

Data availability statement

All data that support the findings of this study are included within the article (and any supplementary files).

ORCID iDs

L M Pérez 0000-0002-2915-309X
D Laroze 0000-0002-6487-8096
V Chaudhary 0000-0003-1461-4073
W J Pasek 0000-0002-0643-450X
A En Naciri 0000-0003-0507-0318
A El Fatimy 0000-0001-6500-7762
E Feddi 0000-0001-6641-3623

References

[1] Chumak A V, Vasyuchka V I, Serga A A and Hillebrands B 2015 *Nat. Phys.* **11** 453
[2] Žutić I, Fabian J and Das Sarma S 2004 *Rev. Mod. Phys.* **76** 323
[3] Joshi V K 2016 *Eng. Sci. Technol., Int. J.* **19** 1503
[4] Hirohata A, Yamada K, Nakatani Y, Prejbeanu I-L, Diény B, Pirro P and Hillebrands B 2020 *J. Magn. Magn. Mater.* **509** 166711
[5] Ohno H 1998 *Science* **281** 951
[6] Fiederling R, Keim M, Reuscher G, Ossau W, Schmidt G, Waag A and Molenkamp L W 1999 *Nature* **402** 787
[7] Ohno Y, Young D K, Beschoten B, Matsukura F, Ohno H and Awschalom D D 1999 *Nature* **402** 790
[8] Ohno H 1999 *J. Magn. Magn. Mater.* **200** 110
[9] Dietl T, Ohno H, Matsukura F, Cibert J and Ferrand D 2000 *Science* **287** 1019
[10] Li X and Yang J 2016 *Natl Sci. Rev.* **3** 365
[11] Titov A *et al* 2005 *Phys. Rev. B* **72** 115209
[12] Ohno H, Munekata H, Penney T, von Molnár S and Chang L L 1992 *Phys. Rev. Lett.* **68** 2664
[13] Ohno H, Shen A, Matsukura F, Oiwa A, Endo A, Katsumoto S and Iye Y 1996 *Appl. Phys. Lett.* **69** 363
[14] Munekata H, Ohno H, von Molnar S, Segmüller A, Chang L L and Esaki L 1989 *Phys. Rev. Lett.* **63** 1849
[15] Oiwa A, Katsumoto S, Endo A, Hirasawa M, Iye Y, Ohno H, Matsukura F, Shen A and Sugawara Y 1997 *Solid State Commun.* **103** 209
[16] Dietl T, Haury A and Merle d'Aubigné Y 1997 *Phys. Rev. B* **55** R3347
[17] Dietl T, Ohno H and Matsukura F 2001 *Phys. Rev. B* **63** 195205
[18] dos Santos R R, Oliveira L E and d'Albuquerque e Castro J 2002 *J. Phys.: Condens. Matter* **14** 3751
[19] Matsukura F, Ohno H, Shen A and Sugawara Y 1998 *Phys. Rev. B* **57** R2037
[20] dos Santos R R, d'Albuquerque e Castro J and Oliveira L E 2003 *J. Appl. Phys.* **93** 1845
[21] Ohno H and Matsukura F 2001 *Solid State Commun.* **117** 179
[22] Szczytko J, Mac W, Twardowski A, Matsukura F and Ohno H 1999 *Phys. Rev. B* **59** 12935
[23] Look D C 1991 *J. Appl. Phys.* **70** 3148
[24] Van Esch A, Van Bockstal L, De Boeck J, Verbanck G, van Steenbergen A S, Wellmann P J, Grietens B, Bogaerts R, Herlach F and Borghs G 1997 *Phys. Rev. B* **56** 13103
[25] Edmonds K W, Wang K Y, Campion R P, Neumann A C, Foxon C T, Gallagher B L and Main P C 2002 *Appl. Phys. Lett.* **81** 3010
[26] Seong M J, Chun S H, Cheong H M, Samarth N and Mascarenhas A 2002 *Phys. Rev. B* **66** 033202
[27] Yu K M, Walukiewicz W, Wojtowicz T, Kuryliszyn I, Liu X, Sasaki Y and Furdyna J K 2002 *Phys. Rev. B* **65** 201303
[28] Yu K M, Walukiewicz W, Wojtowicz T, Lim W L, Liu X, Sasaki Y, Dobrowolska M and Furdyna J K 2002 *Appl. Phys. Lett.* **81** 844
[29] Moriya R and Munekata H 2003 *J. Appl. Phys.* **93** 4603
[30] da Silva A J R, Fazzio A, dos Santos R R and Oliveira L E 2004 *J. Phys.: Condens. Matter* **16** 8243
[31] Maccherozzi F *et al* 2008 *Phys. Rev. Lett.* **101** 267201
[32] Sperl M *et al* 2010 *Phys. Rev. B* **81** 035211
[33] Zhang Y, Xie Z-X, Deng Y-X and Yu X 2015 *Phys. Lett. A* **379** 2745
[34] Badrtdinov D I, Katsnelson M I and Rudenko A N 2024 *Phys. Rev. B* **110** L060409
[35] Zhou J, Shin H D, Chen K, Song B, Duncan R A, Xu Q, Maznev A A, Nelson K A and Chen G 2020 *Nat. Commun.* **11** 6040
[36] Chen C *et al* 2023 *Phys. Rev. Res.* **5** 043089
[37] Gluba L, Yastrubchak O, Domagala J Z, Jakiela R, Andrearczyk T, Żuk J, Wosinski T, Sadowski J and Sawicki M 2018 *Phys. Rev. B* **97** 115201
[38] Gas K, Sadowski J and Sawicki M 2021 *J. Magn. Magn. Mater.* **533** 168012
[39] Golovach V N, Borhani M and Loss D 2006 *Phys. Rev. B* **74** 165319
[40] Chatterjee A, Stevenson P, De Franceschi S, Morello A, de Leon N P and Kuemmeth F 2021 *Nat. Rev. Phys.* **3** 157
[41] Katsaros G, Kukucka J, Vukusic L, Watzinger H, Gao F, Wang T, Zhang J-J and Held K 2020 *Nano Lett.* **20** 5201

[42] Manaselyan A and Chakraborty T 2009 *Europhys. Lett.* **88** 17003
[43] Malik M Z, Kumar D S, Mukhopadhyay S and Chatterjee A 2020 *Physica E* **121** 114097
[44] Boda A, Boyacioglu B, Erkaslan U and Chatterjee A 2016 *Physica E B* **498** 43
[45] Lakaal K, Kria M, El Hamdaoui J, Varsha, Prasad V, Nautiyal V V, El-Yadri M, Pérez L, Laroze D and Feddi E 2022 *J. Magn. Magn. Mater.* **551** 169042
[46] Xiong J-X, Guan S, Luo J-W and Li S-S 2021 *Phys. Rev. B* **103** 085309
[47] Tai C-T, Chiu P-Y, Liu C-Y, Kao H-S, Harris C T, Lu T-M, Hsieh C-T, Chang S-W and Li J-Y 2021 *Adv. Mater.* **33** 2007862
[48] Assali S, Attiaoui A, Vecchio P D, Mukherjee S, Nicolas J and Moutanabbir O 2022 *Adv. Mater.* **34** 2201192
[49] Delaforce J *et al* 2021 *Adv. Mater.* **33** 2101989
[50] van Riggelen F, Hendrickx N W, Lawrie W I L, Russ M, Sammak A, Scappucci G and Veldhorst M 2021 *Appl. Phys. Lett.* **118** 044002
[51] Greilich A, Carter S G, Kim D, Bracker A S and Gammon D 2011 *Nat. Photon.* **5** 702
[52] Lee T D, Low F E and Pines D 1953 *Phys. Rev.* **90** 297
[53] Lee C M 2000 *Phys. Rev. B* **62** 4661
[54] Feddi E, El Haouari M, Assaid E, Stébé B, El Khamkhami J and Dujardin F 2003 *Phys. Rev. B* **68** 235313
[55] This definition corresponds to magnetization as a extensive quantity
[56] Note that this susceptibility has units of [volume]/[μ_0] = J/T^2, since $\mathcal{M}$ is extensive and derivative in definition is taken over B, not H
[57] Zhang H, Sun Y J, Niu E, Yang L H, Shen J, Hu F X, Sun J R and Shen B G 2013 *Appl. Phys. Lett.* **103** 202412
[58] Kim C S and Olendski O 1996 *Phys. Rev. B* **53** 12917
[59] Wang F 2008 Physics with MAPLE: The Computer Algebra Resource for Mathematical Methods in Physics *Physics Textbook* (Wiley) (available at: https://books.google.co.ma/books?id=MeST330ilXQC)
[60] Lang R, Winter A, Pascher H, Krenn H, Liu X and Furdyna J K 2005 *Phys. Rev. B* **72** 024430
[61] Ohya S, Takata K and Tanaka M 2011 *Nat. Phys.* **7** 342
[62] Weber C P, Kittlaus E A, Mattia K B, Waight C J, Hagmann J, Liu X, Dobrowolska M and Furdyna J K 2013 *Appl. Phys. Lett.* **102** 182402
[63] Kulbachinskii V A and Shchurova L Y 2009 *J. Exp. Theor. Phys.* **109** 117
[64] Holmberg H, Lebedeva N, Novikov S, Kuivalainen P, Malfait M and Moshchalkov V V 2007 *Phys. Status Solidi* (a) **204** 791
[65] Wang J, Lv B, Mao H, Zhao Q, Yu J, Liu Y, Zhang Y, Zhu Z and Xing H 2007 *Appl. Phys. Lett.* **91** 052509
[66] Nazmul A M, Sugahara S and Tanaka M 2003 *Phys. Rev. B* **67** 241308
[67] Rushchanskii K Z *et al* 2010 *Nat. Mater.* **9** 649
[68] Helton J S, Matan K, Shores M P, Nytko E A, Bartlett B M, Qiu Y, Nocera D G and Lee Y S 2010 *Phys. Rev. Lett.* **104** 147201
[69] Shaginyan V R, Msezane A Z and Popov K G 2011 *Phys. Rev. B* **84** 060401
[70] Sahu B and Strydom A M 2022 *J. Magn. Magn. Mater.* **541** 168444
[71] Leiner J, Tivakornsasithorn K, Liu X, Furdyna J K, Dobrowolska M, Kirby B J, Lee H, Yoo T and Lee S 2011 *J. Appl. Phys.* **109** 07C307
[72] Evangelisti M, Luis F, de Jongh L J and Affronte M 2006 *J. Mater. Chem.* **16** 2534